



Research Article

Failure Characteristics and Scale in a Sandstone Joint Subjected to Direct Shear Testing: Experimental Investigation with Acoustic Emission Monitoring

Chang Liu,^{1,2} Guang-Liang Feng ,^{1,3} Chun Zhu ,^{1,4} and Ding-Ping Xu¹

¹State Key Laboratory of Geomechanics and Geotechnical Engineering, Institute of Rock and Soil Mechanics, Chinese Academy of Sciences, Wuhan 430071, China

²University of Chinese Academy of Sciences, Beijing 100049, China

³Guangxi Key Laboratory of Disaster Prevention and Engineering Safety, Guangxi University, Nanning 530000, China

⁴School of Earth Sciences and Engineering, Hohai University, Nanjing 210098, China

Correspondence should be addressed to Guang-Liang Feng; glfeng@whrsm.ac.cn

Received 9 April 2022; Revised 25 July 2022; Accepted 15 November 2022; Published 6 December 2022

Academic Editor: Jean Borgomano

Copyright © 2022 Chang Liu et al. Exclusive Licensee GeoScienceWorld. Distributed under a Creative Commons Attribution License (CC BY 4.0).

An in-depth recognition of the failure characteristics and scale of joints is of great significance for the stability assessment in rock engineering. Unfortunately, due to the close fitting of the upper and lower blocks of the joint under direct shear tests, the shear failure of joints are difficult to observe directly during the shear process. Thus, in this work, direct shear tests were carried out on sandstone joints subjected to three levels of normal stress while the acoustic emission (AE) in the rock is synchronously monitored. The failure characteristics of rock joints were then investigated by calibrating the AE system and combining them with the AE location results and shear load curves. A method was established to determine the failure scale of the rock joint that uses the AE moment tensor and first law of thermodynamics. The results show that the degree of failure of the rock joints increases as the normal stress increases. Also, the shear failure of the rock joints is localized and occurs synchronously, rather than sequentially in different areas. The average length of the microfractures formed in the shear process correlates with the average mineral grain size. On the other hand, the maximum length of the microfractures appears to have different values depending on the normal stress present. Our results have significant reference value for the precursory identification of shear disaster in engineering rock masses.

1. Introduction

A rock mass is generally composed of intact rock and joints [1–4]; as a kind of geological weak plane, the occurrence of joints enhances the deformability of rock masses and reduces their strength [5, 6]. When excavation is carried out underground, the rock mass involved will often fracture along discontinuities such as natural joints and bedding planes [7]. This may lead to the occurrence of rockbursts [8–11] or falling blocks [12], threatening the safety of workers and affecting the progress of the engineering work. Therefore, the failure mechanism of rock joints strongly influences the stability of underground engineering [13, 14]. Furthermore, knowledge of the characteristics and scale of the shear failure

occurring in the rock joints is of great significance for understanding the mechanism responsible for shear failure.

In this respect, many scholars have carried out different shear tests to investigate the shear failure mechanism, and much progress has been achieved. Research has mainly focused on shear deformation and characteristics of the peak shear. Barton [1] first used the idea of JRC to define joint roughness and thus proposed a well-known shear strength criterion. Since then, much research has been performed on different aspects. Li et al. [15] conducted shear tests on artificial concrete joint specimens to study their stiffness with respect to shearing. They thus investigated the failure mode of rock joints subjected to different shearing deformation velocities, undulation angles, and normal stresses. They then

proposed a shear stiffness formula for the joints that accounts for the influences of shearing rate and undulation angle. However, little attention has been paid to the characteristics and scale of shear failure in rock joints.

Acoustic emission (AE) occurs when elastic strain energy is instantaneously released as a material undergoes fracturing. The elastic waves produced rapidly propagate through the material and can be detected using an appropriate sensor. AE monitoring is thus an excellent and non-destructive method of analyzing the rock [16–19]. Many scholars have used AE monitoring to investigate the evolution of the failure process in rocks subjected to triaxial or uniaxial compression. The exact location of the failure event producing the AE can be deduced using the difference in arrival time of the elastic wave at different sensors [20–22]. The use of this information has allowed much progress to be achieved in this research area.

Moradian et al. [23] conducted shear tests on joint specimens made of similar materials while monitoring the AE from the samples. Their results proved that AE monitoring is sufficiently accurate to allow the shear failure process in rock joints to be closely followed and can thus be used to analyze the characteristics of the shear failure occurring.

As the AE is generated when the material fractures, the AE signal naturally contains an abundant amount of information about the source of the rock failure. By reversely analyzing the AE signal, the scale of the failure can therefore be evaluated. Some scholars have used the dominant frequency in the AE signal to reflect the scale of the failure. Their general conclusion is that the larger the dominant frequency in the AE signal, the smaller the scale of the failure [24, 25]. However, the dominant frequency can only give a qualitative indication of the failure scale. That is, it cannot be used to quantitatively measure the real length of the failure scale involved.

In this paper, direct shear tests were carried out on sandstone joints while simultaneously monitoring the AE produced. The results were used to study the characteristics and scale of the shear failure occurring in the rock joints. Reasonable values were determined for the parameters of the AE system to ensure that the AE-monitoring system is effective. The results of the direct shear tests were combined with the AE information to investigate the failure characteristics and failure scale of the rock joints. The results further our understanding the shear failure mechanisms of joint rocks. They may also constitute an important reference for identifying precursory signs of impending shear-induced disaster in engineering rock masses.

2. Preparation of Joint Specimens and Testing Scheme

2.1. Specimen Preparation. The sandstone used in this paper is from the Xiaohong Mountain Processing Plant in Wuhan, Hubei Province, China. It is composed mainly of quartz, feldspar, and a very small amount of white mica. The physical and mechanical parameters of the sandstone used in our tests are listed in Table 1. Uniaxial compression tests were performed on cylinders made from the sandstone measuring 100 mm (height) by 50 mm (diameter). The UCS, Young's

TABLE 1: Physical and mechanical parameters of sandstone.

| Parameter | Index | Unit | Value |
|-------------------------------|------------|---------------------------------|-------|
| Uniaxial compressive strength | UCS | MPa | 44.63 |
| Young's modulus | E | GPa | 10.36 |
| Shear modulus | G | GPa | 4.18 |
| Poisson's ratio | ν | — | 0.24 |
| Tensile strength | σ_t | MPa | 1.14 |
| Density | ρ | g/cm^3 | 2.27 |
| Elastic wave velocity | V_p | m/s | 2715 |
| Friction coefficient | μ | — | 0.37 |
| Fracture toughness of type II | K_{II} | $\text{MPa}\cdot\text{m}^{0.5}$ | 2.21 |
| Fracture toughness of type I | K_{IC} | $\text{MPa}\cdot\text{m}^{0.5}$ | 0.72 |
| Porosity | n | — | 19.2% |

modulus, shear modulus, and Poisson's ratio of the sandstone were thus obtained. The tensile strength of the sandstone was obtained by performing Brazilian splitting tests. The density of the sandstone was measured by carrying out physical measurements, as were the velocity of elastic waves and porosity in the material. The sandstone's type-II fracture toughness was determined by carrying out a shear box test; the type-I fracture toughness was determined by performing a three-point bending test.

Sandstone joint specimens were fabricated using a 3D-scanning and 3D-engraving technique. A natural joint in specimen (Figure 1(a)) was first scanned using 3D-scanning equipment (Figure 1(b)). The digital point cloud data thus obtained were subsequently processed to generate a 3D digital model of the joint (Figure 1(c)). This model was then imported into a 3D-engraving machine and used to engrave a rectangular block thus generating the upper block of a joint specimen. Another rectangular block was then engraved with the inverted pattern of the joint to obtain the lower block of the joint. Together, the lower and upper blocks created form a complete joint specimen ready for shear testing. Further details of the engraving process are given in the paper by Jiang et al. [2].

The joint specimen size is 150 mm \times 120 mm \times 150 mm (Figure 2(a)). The joints are relatively rough with a roughness (JRC value) between 12 and 14. In all, a total of 9 joint specimens (Figure 2(b)) were made to use in the shear tests (three different normal stresses were employed, each test being repeated three times).

2.2. Testing Scheme. According to the research of Jiang et al. [26], joints subjected to different normal stresses have different failure characteristics. In our tests, three values of normal stresses were adopted: 0.15 MPa (a low stress corresponding to 0.33% of the UCS value), 0.50 MPa (an intermediate stress which is 1.1% of the UCS), and 2.0 MPa (a high normal stress equal to 4.5% of the UCS). The 9 joint specimens were labeled S-NR-1 to S-NR-9 (Table 2) forming 3 groups of samples each consisting of specimens subjected to low, intermediate, and high normal stress.

The shear tests were carried out on the RMT-150C machine from the Institute of Rock and Soil Mechanics,

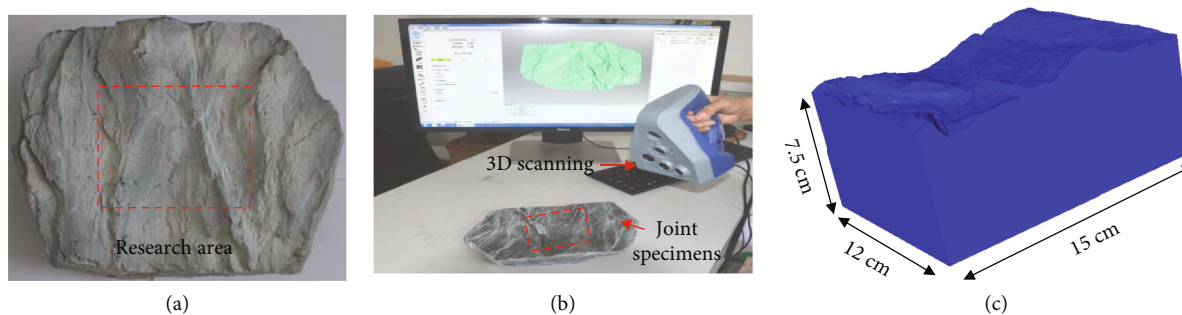


FIGURE 1: Acquisition of rock joint digital model. (a) A natural joint in a rock specimen to use as a template. (b) The 3D-scanning process. (c) Rock joint digital model.

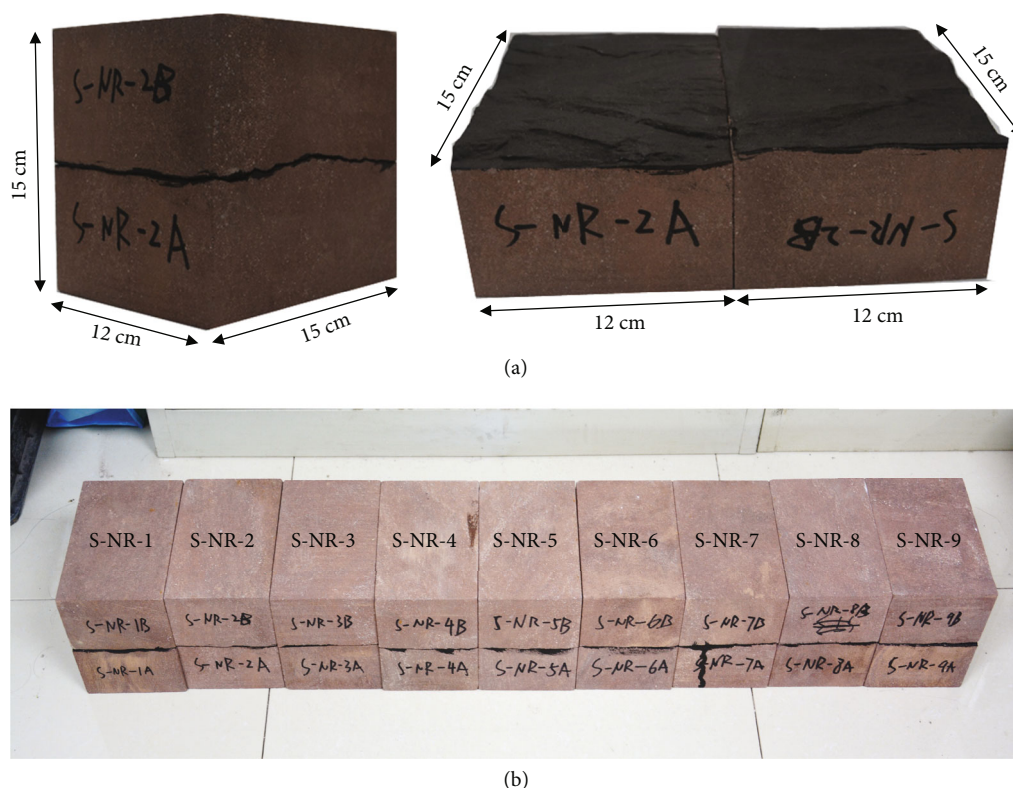


FIGURE 2: Details of the sandstone joint specimens. (a) Schematic diagram of one joint specimen and (b) 9 joint specimens.

TABLE 2: Normal stress scheme.

| Specimen | Group | Normal stress (MPa) |
|----------|-------|---------------------|
| S-NR-1 | 1 | 0.15 |
| S-NR-2 | 1 | 0.5 |
| S-NR-3 | 1 | 2 |
| S-NR-4 | 2 | 0.15 |
| S-NR-5 | 2 | 0.5 |
| S-NR-6 | 2 | 2 |
| S-NR-7 | 3 | 0.15 |
| S-NR-8 | 3 | 0.5 |
| S-NR-9 | 3 | 2 |

Chinese Academy of Sciences. The normal stress and shear loads applied were controlled via a servo-controlled system. The normal stress was applied first (to the required value) and the shear load was subsequently applied thereafter (Figure 3(a)).

The shear tests were under constant normal stress with displacement controlled at a loading rate of 0.005 mm/s, and the maximum displacement was 12 mm, which can ensure the complete failure of the sandstone joints and obtain the whole stage test curve of the shear failure process.

The AE-monitoring equipment employed was manufactured by the PAC Company. It consists of 16 AE-monitoring channels, each having 18 A/D accuracy. The equipment is capable of fast data acquisition and stable signal recording, making it ideal for directly recording the AE signals produced during the shear tests.

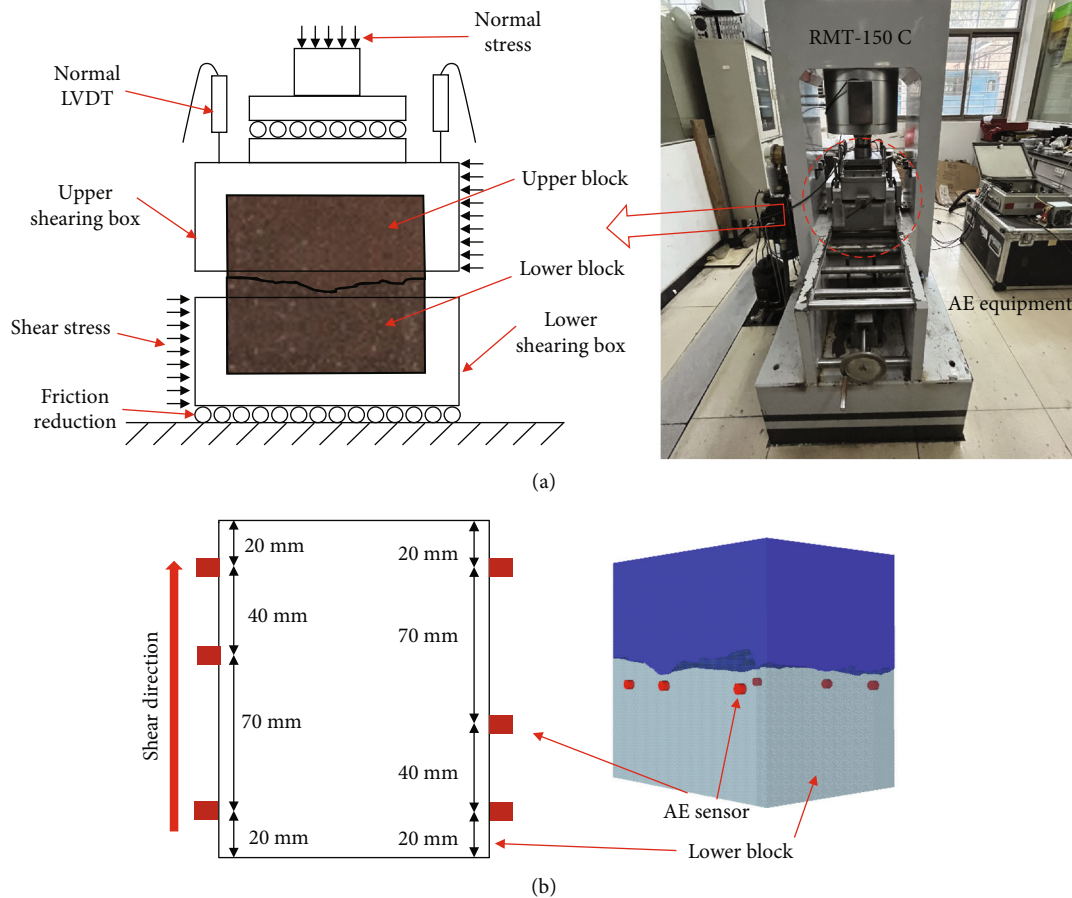


FIGURE 3: Details of the testing system. (a) Shear equipment. (b) Layout of the AE sensors.

Nano-30 AE sensors (also produced by PAC) were employed in the experiments. These have high acquisition sensitivity and good frequency response over the range 125–750 kHz. As the joints mainly fail near the joint surface, the AE sensors were positioned in a plane close to the joint (Figure 3(b)). As can be seen, a total of six AE sensors were employed. They were equally distributed on both sides of the lower block in the shear direction (i.e., there were three AE sensors on each side). The six sensors all lie in the same horizontal plane and are located on the two sides of the specimen in the shearing direction, thus enclosing the entire joint surface. This is to optimize their ability to collect the fracturing signals produced during the shearing process as much as possible. The dislocation arrangement employed is chosen to make the difference in distance between any point in the surface of the rock joint and six sensors as large as possible. This reduces the possibility that the matrix used to calculate position suffers from deformity.

3. Calibration of the AE System

The elastic wave released when the rock undergoes fracturing and propagates to the AE sensor through the rock. The AE system collects the signal above the threshold and converts the signal into a discrete signal according to the sampling

frequency and stores it in the system. The location of the fracture source is determined by the arrival time of the elastic wave signal and the coordinates of the sensor in the AE system. During the whole test, some parameters of the AE system are unique depending on the test scheme used (e.g., the correspondence between sensor number, channel number, and sensor coordinate position). These parameters do not need to be calibrated and only unique values can be determined by user.

However, the AE threshold and the sampling frequency have a certain range of values, which need to be calibrated in combination with the test environment and the spectrum range of the fracture signal. These two parameters can strongly influence the AE-monitoring results and even invalidate them. If the threshold value is too high, the system may fail to record some important signals of the rock failure process. On the other hand, if the threshold value is too low, the AE signal may be swamped with noise making the subsequent analysis difficult to perform.

The AE sampling frequency is the number of samples recorded per second when the elastic wave is converted from an electrical signal into a digital signal. If the sampling frequency is too high, the amount of signal data generated will be huge. This may lead to system lag or error leakage when monitoring is carried out over a long period of time. Conversely, if the sampling frequency is too low, the signal will

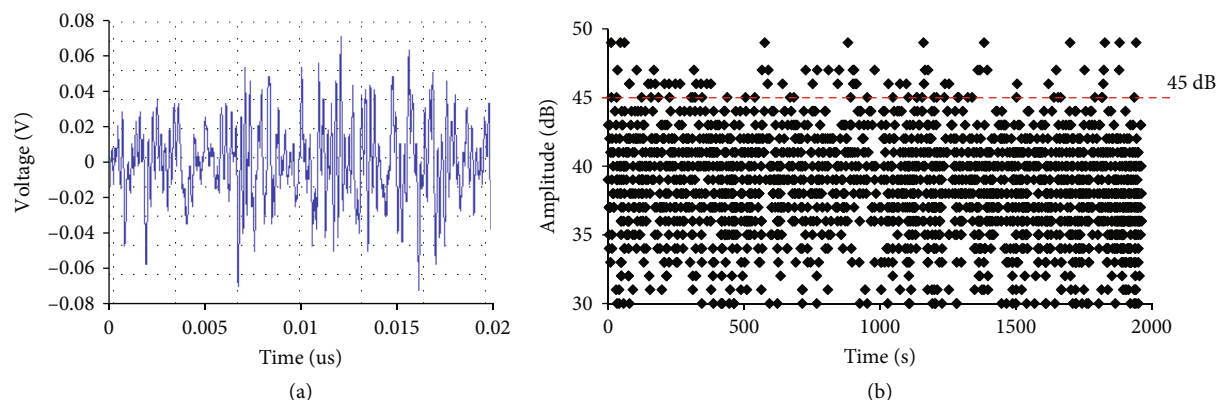


FIGURE 4: Hydraulic noise signal. (a) Signal waveform. (b) Signal amplitude distribution.

be distorted and large errors will be produced in the subsequent analysis.

Thus, reasonable values must be selected for these two parameters in order to ensure that the failure signals are efficiently and accurately recorded. In this way, the characteristics and scale of the shear failure occurring in the specimens derived via the subsequent analysis will be reliable.

The threshold value of the AE-monitoring system corresponds to the signal amplitude at which AE signals of lower amplitude are blocked. Only if the amplitude of the signal is higher than the threshold will the signal be recorded by the acquisition system. Scholars have adopted different AE threshold values in their experiments. Some have adopted a threshold value of 52 dB [27], others have used 50 dB [23], and many have chosen to use 45 dB [28–32]. However, no reasons were provided for using these threshold values. Therefore, we decided to determine a more reasonable value for the AE threshold value by analyzing the noise in the laboratory and setting up a blank sensor.

In our tests, the shear load is applied to the specimen using a hydraulic pressure system. Therefore, the noise in the laboratory is mainly due to environmental white noise and noise from the hydraulic system. The amplitude of the environmental white noise is relatively low and so this source can be easily blocked using a threshold based on the hydraulic noise. The latter noise has a wide amplitude distribution and so it is necessary to intercept it by setting an appropriate threshold value. In order to determine the actual amplitude distribution of the hydraulic noise in the laboratory, a blank AE sensor with a threshold value of 30 dB was attached to the shear equipment. Shear tests were then carried out (using the highest normal stress value employed in our tests) so as to obtain the shape of the noise signal (Figure 4(a)) and its amplitude distribution (Figure 4(b)). It can be seen that the amplitude distribution of the hydraulic noise signal lies in the range 30–50 dB. Moreover, a threshold value of 45 dB can filter out 94% of the hydraulic noise.

Figure 5 shows the amplitude distribution of the signals produced due to the shear failure of a joint rock specimen. The figure indicates that the amplitude distribution above 45 dB conforms to a normal distribution with an expectation value of 51 dB and variance of 30.21. Furthermore, based on this normal distribution, it can be calculated that the propor-

tion below 45 dB corresponds to 15.8% of the total distribution. Thus, a threshold value of 45 dB will ensure that most of the rock failure signals (84.2%) will be detected by the system. It will also ensure that most of the noise is filtered out. Overall, therefore, a threshold setting of 45 dB is both reasonable and reliable.

Theoretically, the greater the sampling frequency, the better the discrete data represent the real shape of the continuous signal. However, if the sampling frequency is too high, the amount of data produced (and hence memory required) will be huge. At the same time, the demand placed on the acquisition system may exceed the limits of its acquisition ability if there is a surge in the AE signal. Thus, some (clearly important) signals may not be recorded. Similarly, too low of a sampling frequency will lead to the signal being distorted. This can lead to inaccurate or invalid monitoring results.

The sampling theory states that the sampled data can accurately describe a continuous signal provided the sampling frequency employed exceeds two times the maximum frequency contained in the original signal. For this work, we collected a large number of real rock failure signals via tests. The time-domain data can then be transformed into the frequency domain (Figure 6) by subjecting it to discrete Fourier transformation.

Having considered a large number of rock failure signals (Figure 7), it is apparent that the AE frequencies in the rock failure data are mainly concentrated between 150 and 350 kHz. Moreover, the maximum frequency does not exceed 500 kHz; this is in line with the research results of many scholars [24, 30]. According to sampling theory, therefore, the sampling frequency used to detect the AE signal should be set to 1 million sample times per second (1 MHz) in order to fully ensure that the monitoring results are effective.

In conclusion, an AE threshold value of 45 dB and sampling frequency of 1 MHz can be expected to work very well in our experiments.

4. Calculation Method of Failure Scale Using AE Information

The AE phenomenon is associated with the failure processes occurring in the material and is a rich source of information about the fracturing processes responsible. The AE signals

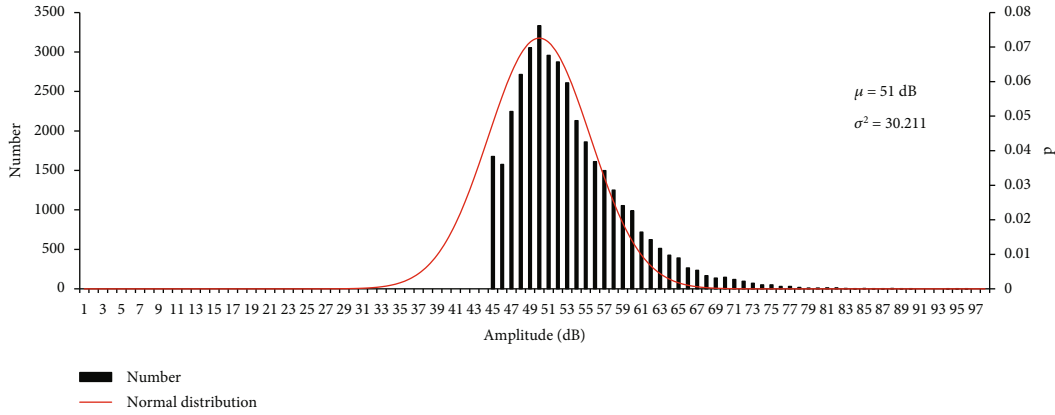


FIGURE 5: Distribution of the amplitudes of the rock failure signals.

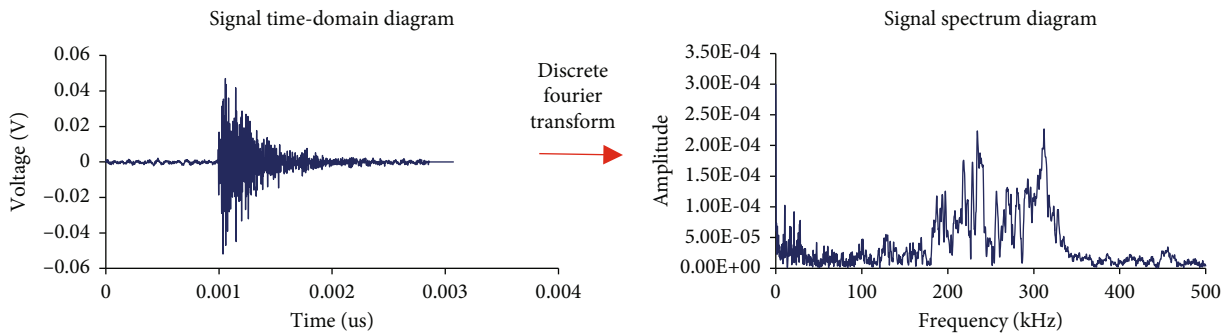


FIGURE 6: Spectrum transformation of a typical rock failure signal.

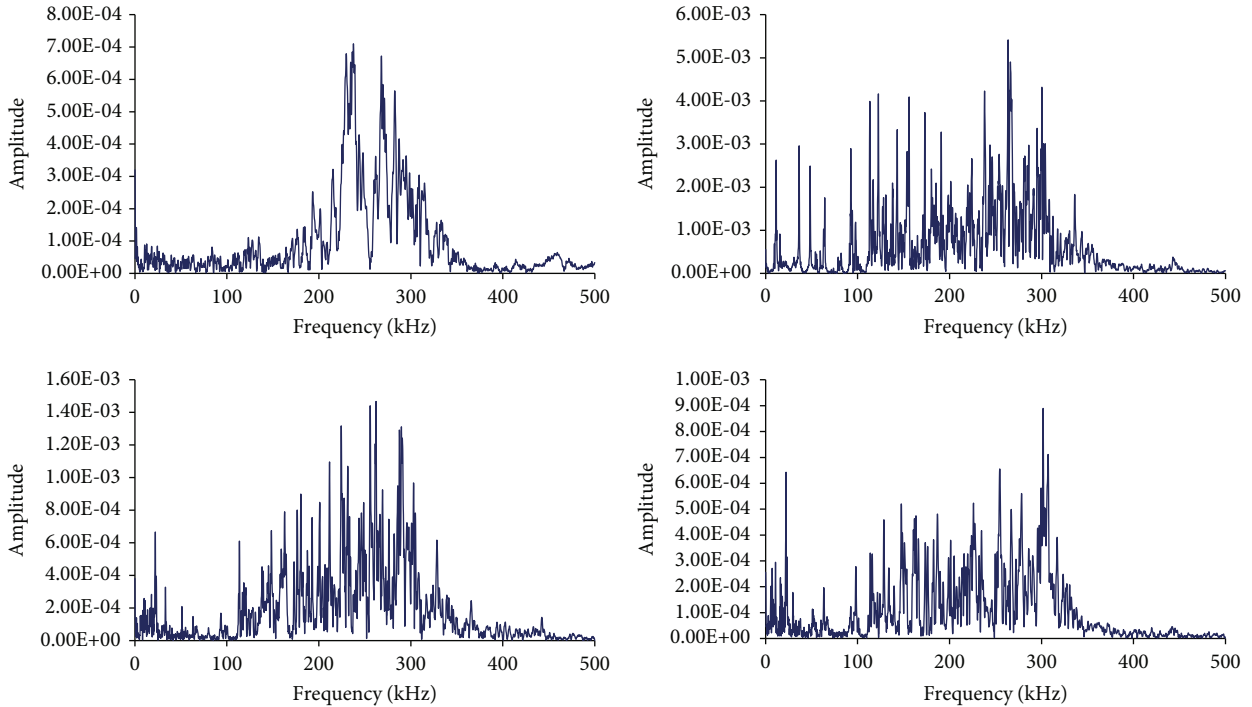


FIGURE 7: Spectrum diagram of real rock failure signals.

released by failure processes of different scales will also be different. Therefore, it should be possible to evaluate the failure scale by analyzing the AE information.

In this paper, we establish a method of calculating the failure scale using the AE information. The method involves combining the AE moment tensor with the first law of

thermodynamics and allows the length of the microfractures generated in the failure process to be calculated, thus giving a true reflection of the fracture scale in the material.

When a rock is subjected to an external force, microfracturing may occur and the energy thus released can be detected using an AE sensor. First, the AE signals received are processed to yield the kinetic energy of the microfracture source. This information is then combined with the first law of thermodynamics to calculate the lengths of the microfractures.

Regardless of any thermal effects, the generation of a microfracture must conform to the first law of thermodynamics. We thus have

$$E_i = E_a + E_d + E_k, \quad (1)$$

where E_i is the internal energy (i.e., the total work done by all the stresses acting on the microfracture surface), E_a is the surface energy on the microfracture surface, E_d is the dissipated energy on the microfracture surface, and E_k is the kinetic energy on the microfracture surface.

E_a is the energy required to overcome molecular cohesion during fracture. The dissipated energy E_d is mainly caused by plastic deformation and sliding friction. E_k is the kinetic energy of vibration on the fracture surface.

The kinetic energy E_k of the microfracture source radiates outwards in the form of an elastic wave. Its value is proportional to the square integral of the particle velocity spectrum and can be calculated using the AE waveform envelope. Yamada et al. [33] have provided a formula that can be used to calculate the kinetic energy:

$$E_k = 4\pi L^2 \rho V_p \left(\frac{\langle R_p \rangle}{R_p} \right)^2 \int_0^{t_d} (C_v v(t))^2 dt, \quad (2)$$

$$C_v = \frac{R_p M_0}{1/3 \text{tr}(M) + R_p M_0}, \quad (3)$$

where L is the distance between the microfracture source and AE sensor, ρ is the density of the rock, V_p is the elastic wave velocity in rock, $\langle R_p \rangle$ is the average propagation coefficient of all the sensors, R_p is the propagation coefficient of a particular sensor, C_v is the correction term of the volumetric component, $v(t)$ is the particle velocity waveform of the fracturing source, and t_d is the duration of the signal.

In order to reduce the gap between the surface of the sensor and the surface of the rock sample and enhance the propagation ability of the elastic wave, a coupling agent is generally used between the rock sample and the sensor. The propagation process of the elastic wave is from the rock to the coupling agent and finally to the AE sensor. As elastic waves propagate between two different media, their amplitude changes, thus requiring a propagation coefficient to correct the amplitude of the signal received by the sensor. Based on the elastic wave dynamics, the propagation coefficient of the sensor R_p can be determined as

$$R_p = \frac{2w \cos \theta_i}{w \cos \theta + \sqrt{q^2 - \sin^2 \theta}}, \quad (4)$$

where $w = \rho_c / \rho$ and $q = V_c / V_p$, ρ_c is the density of the coupling agent, V_c is the elastic wave velocity in the coupling agent, and θ_i is the angle between the direction of elastic wave propagation and the normal to the sensor surface.

The symbol M in Equation (3) denotes the moment tensor of the AE source inversion. It can be decomposed into two parts:

$$M = \begin{pmatrix} M_{11} & 0 & 0 \\ 0 & M_{22} & 0 \\ 0 & 0 & M_{33} \end{pmatrix} = \frac{1}{3} \text{tr}(M) \begin{pmatrix} 1 & 0 & 0 \\ 0 & 1 & 0 \\ 0 & 0 & 1 \end{pmatrix} + \begin{pmatrix} m_{11} & 0 & 0 \\ 0 & m_{22} & 0 \\ 0 & 0 & m_{33} \end{pmatrix}, \quad (5)$$

where $\text{tr}(M) = M_{11} + M_{22} + M_{33}$ is the trace of the matrix M and m_{11} , m_{22} , and m_{33} are the deviatoric eigenvalues of the matrix M , $M_0 = |m_{11} + 0.5m_{33}|$.

The matrix M can be determined by six effective signals involved in AE positioning:

$$M = \begin{pmatrix} a_{11} & a_{12} & a_{13} \\ a_{12} & a_{22} & a_{23} \\ a_{13} & a_{23} & a_{33} \end{pmatrix}, \quad (6)$$

$$u(x) = C_s \frac{R_p}{L} (r_1 \ r_2 \ r_3) \begin{pmatrix} a_{11} & a_{12} & a_{13} \\ a_{12} & a_{22} & a_{23} \\ a_{13} & a_{23} & a_{33} \end{pmatrix} \begin{pmatrix} r_1 \\ r_2 \\ r_3 \end{pmatrix}, \quad (7)$$

where $u(x)$ is the amplitude of the signal received at the AE sensor, C_s depends on the sensitivity of the sensor, which can be determined by the lead break test, and $(r_1 \ r_2 \ r_3)$ is the direction vector from the AE source to the sensor.

As indicated in Equation (6), the matrix M is symmetric. Through the coordinates of six sensors involved in positioning and the received signal amplitude, a_{11} , a_{12} , a_{13} , a_{22} , a_{23} , and a_{33} in the matrix M can be solved; it can be diagonalized and changed as follows:

$$\begin{pmatrix} a_{11} & a_{12} & a_{13} \\ a_{12} & a_{22} & a_{23} \\ a_{13} & a_{23} & a_{33} \end{pmatrix} \Rightarrow \begin{pmatrix} M_{11} & 0 & 0 \\ 0 & M_{22} & 0 \\ 0 & 0 & M_{33} \end{pmatrix} = M. \quad (8)$$

Thus, the correction value of the volumetric component C_v in Equation (4) can be solved.

The AE signal is collected and stored by converting the particle vibration velocity (m/s) into a voltage signal (mV). Therefore, there is a relationship between the particle vibration velocity waveform $v(t)$ and corresponding voltage signal waveform $u(t)$:

$$v(t) = \frac{u(t)}{St}, \quad (9)$$

where St is the sensitivity value of the sensor (in dB). The sensor manufacturer will conduct a sensitivity test on the sensor and give a sensitivity curve, and the maximum amplitude value on the sensitivity curve is used as the sensitivity value. When there are several AE sensors, the average value of the sensitivity is taken as the sensitivity value of the overall system.

Therefore, Equation (3) can be converted to

$$E_k = 4\pi L^2 \rho V_p C_v^2 R_p^2 \frac{1}{St^2} \int_0^{t_d} u(t)^2 dt. \quad (10)$$

During the AE-monitoring process, the monitoring system can automatically calculate the RMS value of the signal. That is, it finds the root-mean-square value of the signal over the sampling time:

$$RMS = \sqrt{\frac{1}{t^d} \int_0^{t_d} u(t)^2 dt}. \quad (11)$$

Inserting Equation (11) into Equation (10) yields

$$E_k = 4\pi L^2 \rho V_p C_v^2 R_p^2 \frac{1}{St^2} RMS^2 t^d. \quad (12)$$

As the internal energy E_i , surface energy E_a and dissipated energy E_d of tensile fracture and shear fracture are different. Thus, different calculation methods are required for tensile and shear fracturing. Thus, the two different cases need to be discussed separately.

Zhang et al. [34] managed to derive an equation for the internal energy E_i of a shear fracture by assuming that: (i) the rock mass is homogeneous and isotropic, (ii) the shear fracture range is a disk of radius a , and (iii) the shear fracture occurs instantly:

$$E_i = \frac{1.52\pi^2 (0.66\tau^2 + 0.68\tau u \sigma_n - 1.34u^2 \sigma_n^2) a^2}{4G}, \quad (13)$$

where τ is the shear stress on the shear fracture surface, u is the effective friction coefficient, G is the shear modulus, and σ_n is the normal stress on the shear fracture surface. Meanwhile, the dissipated energy E_d can be expressed in the form [24]

$$E_d = \frac{1.52\pi^2 (\tau u \sigma_n - u^2 \sigma_n^2) a^2}{2G}. \quad (14)$$

Furthermore, the surface energy on the shear fracture surface can be expressed in the form [35]

$$E_a = \frac{2\pi(1-\nu^2)K_{II}^2 a^2}{E}, \quad (15)$$

where ν is Poisson's ratio, K_{II} is the type-II fracture toughness, and E is Young's modulus.

Combined with Equations (2) and (12)–(15), the failure scale of the shear fracture can be expressed in the form

$$d_s = 2a = 2\sqrt{\frac{4L^2 \rho V_p C_v^2 R_p^2 ((1/St^2)RMS^2 t^d)}{(1.0032\pi(\tau - u\sigma_n)^2/4G) - (2(1-\nu^2)K_{II}^2/E)}}. \quad (16)$$

When tensile fracturing occurs, the dissipated energy E_d can be ignored as sliding does not occur between the fracture surfaces [35]. The internal energy E_i of the tensile fracture surface can be expressed in the form [36]

$$E_i = \frac{(1-\nu^2)\pi\sigma_n^2 a^2}{E}. \quad (17)$$

Surface energy E_a on tensile fracture surface can be expressed in the form

$$E_a = \frac{2(1-\nu^2)K_{IC}^2 a^2}{E}, \quad (18)$$

where ν is Poisson's ratio, K_{IC} is the type-I fracture toughness, and E is Young's modulus.

Combination of Equations ((2)), ((12)), ((17)), and ((18)) yields the following expression for the failure scale of the tensile fracture:

$$d_t = 2a = 2\sqrt{\frac{4\pi L^2 \rho V_p C_v^2 R_p^2 ((1/St^2)RMS^2 t^d)}{((1-\nu^2)\pi\sigma_n^2/E) - (2(1-\nu^2)K_{IC}^2/E)}}. \quad (19)$$

Equations (16) and (19) can calculate the failure scale for tensile fracture and shear fracture. The calculation process is to first distinguish the fracture type and then calculate the failure scale based on the corresponding equation. The moment tensor of the AE source inversion is able to identify the fracture type, and the matrix M can be determined by six effective signals involved in the AE positioning (Equation (6)). The three eigenvalues of the matrix M are λ_{\max} , λ_{int} , and λ_{\min} . The fracture type of the failure can be determined based on the three eigenvalues (Equations (20), (21), and (22)).

$$\frac{\lambda_{\max}}{\lambda_{\max}} = X + Y + Z, \quad (20)$$

$$\frac{\lambda_{\text{int}}}{\lambda_{\max}} = -0.5Y + Z, \quad (21)$$

$$\frac{\lambda_{\min}}{\lambda_{\max}} = -X - 0.5Y + Z. \quad (22)$$

If X is greater than 0.6, it is shear fracture, if X is less than 0.4, it is a tensile fracture, and if X is between 0.4 and 0.6, it is a mixed tensile-shear fracture. The failure scale of the shear fracture is calculated by Equation (16); the failure scale of the tensile fracture is calculated by

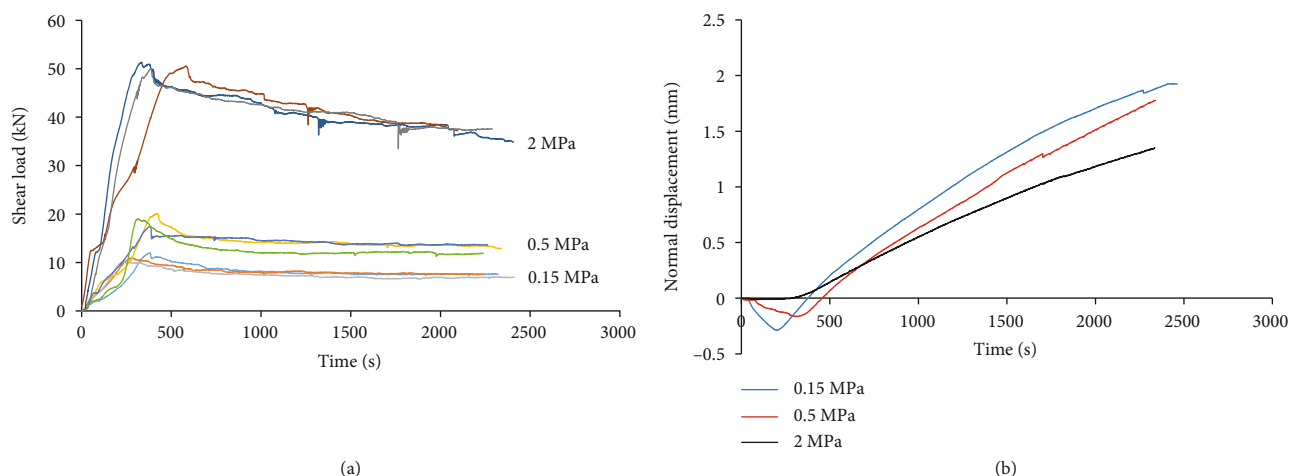


FIGURE 8: Results of the shear tests: (a) shear load curves and (b) normal displacement curves.

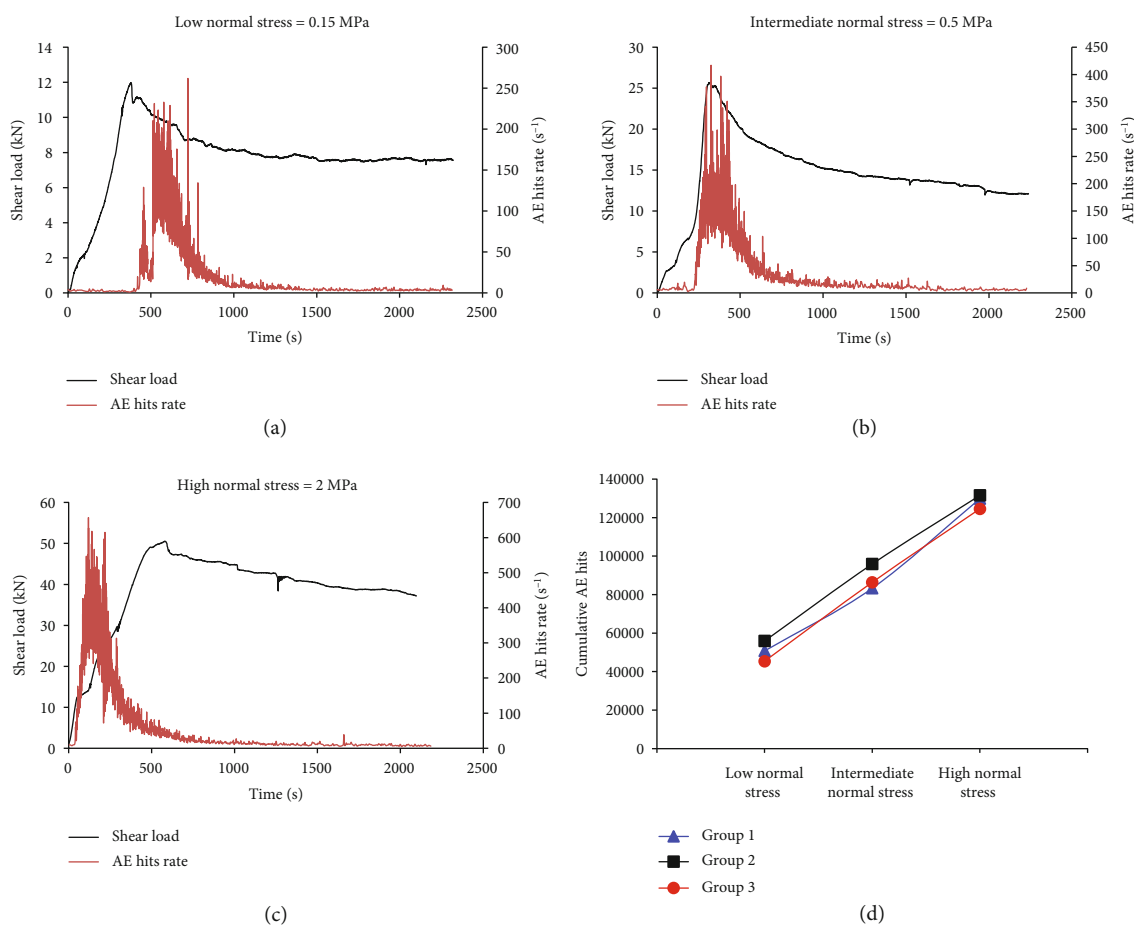


FIGURE 9: AE hit rate curves of sandstone joints: (a) 0.15 MPa, (b) 0.5 MPa, and (c) 2 MPa. (d) Cumulative AE hits under three kinds of normal stresses.

Equation (19); the failure scale of the mixed tensile-shear fracture is the average value of Equations (16) and (19).

In summary, the failure scale of fractures can be deduced by analyzing the signals received by the AE sensors and combining the first law of thermodynamics.

5. Results and Analysis

5.1. Shear Failure Characteristics of Rock Joints. The direct shear tests (and simultaneous AE monitoring) were carried out on the jointed sandstone specimens using three applied

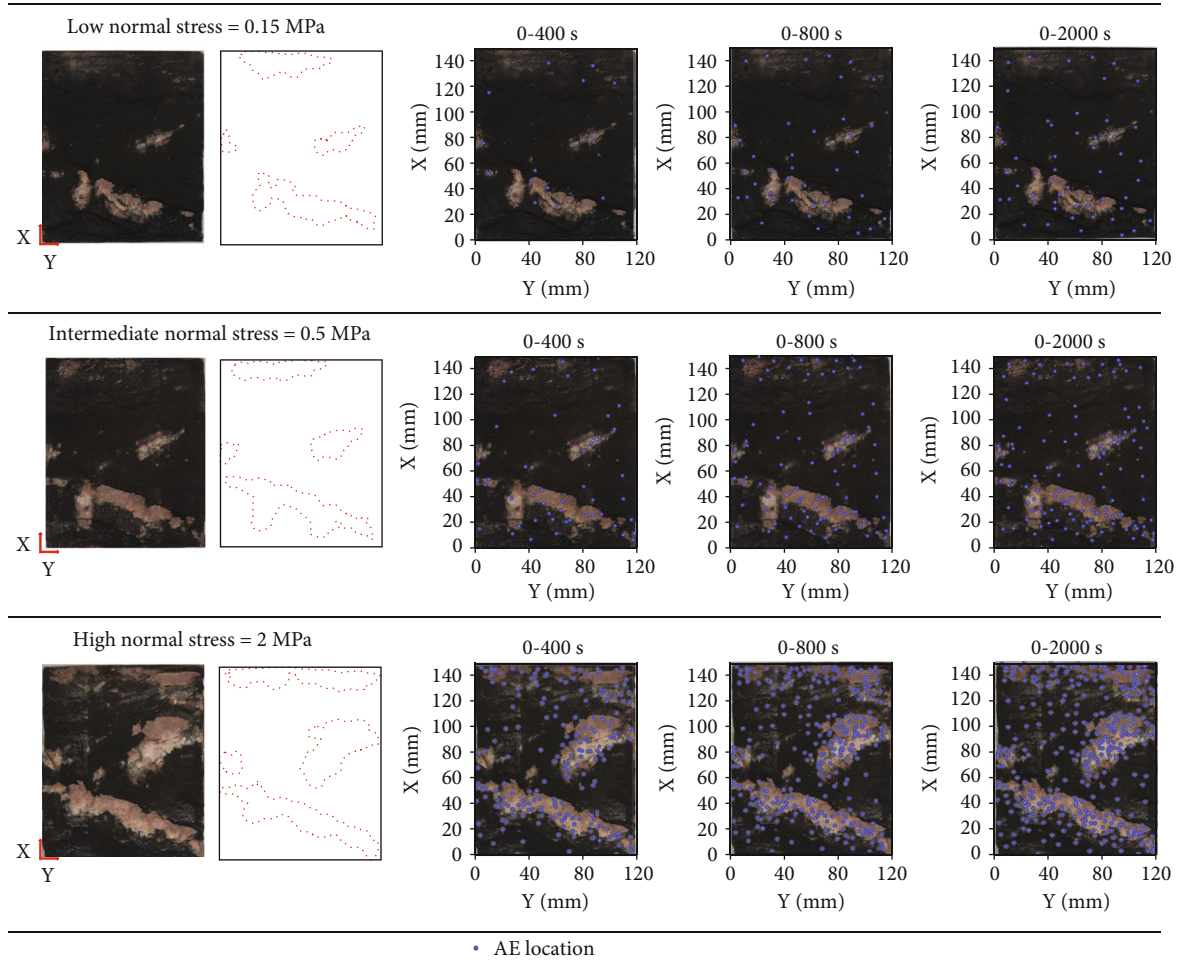


FIGURE 10: Spatiotemporal evolution of the shear failure of sandstone joints subjected to different normal stresses.

normal stresses. The results of the shear tests are shown in Figure 8 and the corresponding AE data are demonstrated in Figure 9.

The shapes of the shear curves presented in Figure 8(a) are essentially the same regardless of the normal stress applied to the sandstone joint specimen. In each case, as the shear displacement increases, the shear load gradually increases, reaches a peak value, and then gradually decreases to a constant residual value. In addition, the maximum shear load recorded clearly increases with the magnitude of the applied normal stress.

According to the normal displacement curves shown in Figure 8(b), only a small amount of deformation occurs in the normal direction when a normal stress of 2 MPa is applied. As the normal stress is reduced to 0.5 MPa and then to 0.15 MPa, the maximum normal deformation increases accordingly. Thus, the applied normal stress strongly inhibits the normal deformation of the jointed sample.

Figure 9(a) shows that the maximum number of AE events recorded per second by the monitoring system is 261 hits/s when the low normal stress (0.15 MPa) is used. Moreover, as the normal stress is increased, the maximum AE activity also increases, reaching peak values of 416 hits/s when the intermediate stress (0.5 MPa, Figure 9(b)) is used

and 657 hits/s when the high stress (2 MPa, Figure 9(c)) is used. Thus, the number of AE hits recorded per second increases as the applied normal stress increases. This variation is presented more clearly in Figure 9(d) which shows that the cumulative number of AE hits recorded clearly increases with increasing normal stress.

The above results show that the peak shear load increases as the normal stress is increased. The severity of the shear failure also increases. The surfaces of the joints in the sandstone are naturally red in color. To help show which parts of the joint are undergoing failure, black ink was applied to the surface of the joint before shear testing was performed. The evolution of the shear failure process could then be followed by combining photographs of the specimen surfaces after testing with the results of the AE location tests. The results are shown in Figure 10.

The joints used in our tests appear to undergo failure in four main areas (highlighted by the red dotted lines shown in Figure 10 which correspond to regions in which the black ink has clearly been disturbed). No other areas appear to undergo failure as the normal stress is increased but the sizes of the main four failure areas can be seen to grow in magnitude. This indicates that the joints undergo shear failure in certain specific localized regions. This is undoubtedly caused

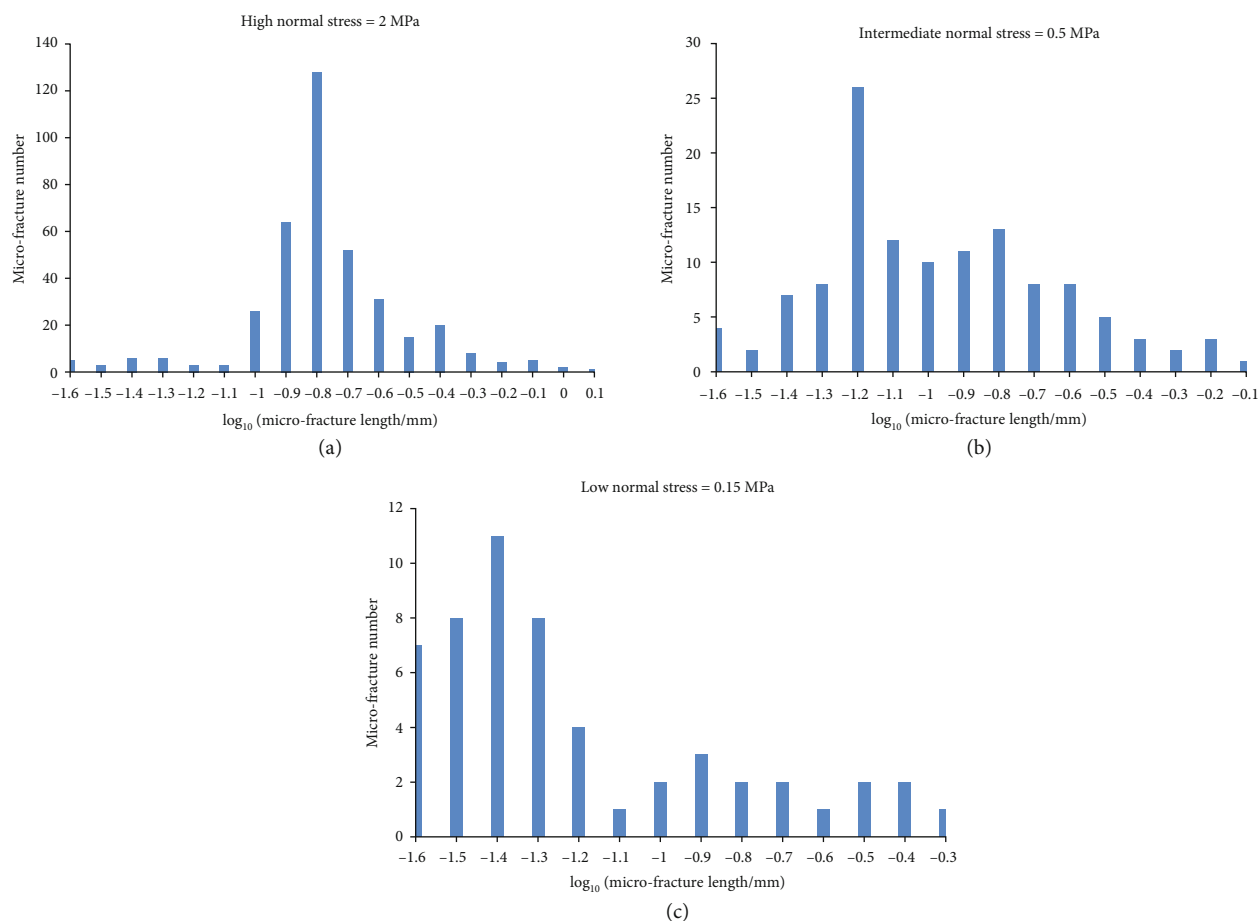


FIGURE 11: Distributions of the lengths of the microfractures produced in sandstone joints subjected to normal stresses of (a) 2 MPa, (b) 0.5 MPa, and (c) 0.15 MPa.

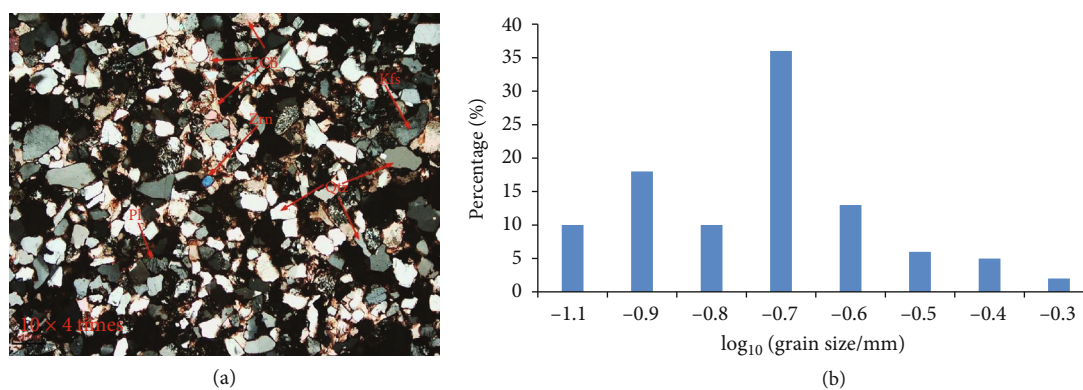


FIGURE 12: (a) Photomicrograph of the sandstone captured using a scanning electron microscope. (b) Distribution of the sizes of the grains in the sandstone.

by the inhomogeneity of the joint surface which effectively leads to a distribution of shear angles being formed on the joint's surface.

In Figure 10, the complete shearing process is divided into three stages corresponding to 0–400 s (mainly corresponding to the prepeak region of the shear curve), 400–800 s (region near the peak), and 800–2000 s (region where the residual shear loading occurs). It can be seen that the number of AE events occurring in the vicinity of each of

the four failure areas increase in each stage. This indicates that the four regions undergo failure synchronously as the shear displacement is increased. In other words, it is not a case of one area failing first and then other areas failing subsequently. That is, the surface as a whole undergoes shear failure (in localized areas) at the same time.

In summary, the failure degree of rock joints increases with the increase of normal stress; shear failure characteristics of rock joints have localized and synchronous failure.

5.2. Shear Failure Scale of Rock Joints. The Nano-30 AE sensors used in our experiments have a sensitivity of 58 dB. The density of the coupling agent is 0.98 g/cm^3 , and the elastic wave velocity in the coupling agent is 2210 m/s. According to Section 4, the length of microfracture in the shear process of sandstone joints can be calculated.

Figure 11 shows the distributions of the lengths of the microfractures thus derived. It should be noted that as the microfractures produced can vary widely in length, logarithmic length scales are adopted in Figure 11.

The microfractures generated in sandstone joints subjected to a normal stress of 2 MPa have lengths ranging from 0.02 mm to 1.19 mm (or -1.6 to 0.1 using the log scale adopted in Figure 11(a)). Their average length is 0.215 mm. Those generated in joints subjected to a normal stress of 0.5 MPa (Figure 11(b)) lie in the range 0.02–0.75 mm (-1.6 to -0.1 using the log scale), and their average length is 0.145 mm. Finally, when a normal stress of 0.15 MPa is used (Figure 11(c)), the microfractures generated have lengths in the range 0.02–0.49 mm (-1.6 to -0.3 using the log scale) and their average length is 0.094 mm.

Overall, it can be seen that the maximum length of the microfractures generated increases as the normal stress applied to the joint is increased. As a result, the average microfracture length also gradually increases.

Scanning electron microscopy and mineral grain identification experiments were also carried out on the sandstone used in the shear tests (Figure 12). The results indicate that the sandstone is mainly made of quartz (60%) with grain sizes ranging from 0.06 mm to 0.45 mm. It also contains a small amount (5%) of feldspar with grain sizes ranging from 0.06 mm to 0.25 mm. There is also a small amount of dolomite present. Overall, the grains in the sandstone fall in the size range 0.06–0.45 mm (or -1.1 to 0.3 using the log scale adopted in Figure 12(b)) and the average grain size is 0.21 mm.

As shown above, the average length of the microfractures generated when shear tests were carried out using a normal stress of 2 MPa is 0.215 mm. When a lower normal stress of 0.5 MPa is applied, the average crack length decreases to 0.145 mm. These averages are essentially consistent with the average grain size in the sandstone. If the normal stress is reduced even further (to 0.15 MPa), then the average length of the microfractures generated (0.094 mm) falls to roughly half the average grain size. This is still consistent with the conclusion that the average length of the microfractures is of the same order as the average grain size of the mineral components [34].

It should be noted that the maximum microfracture length when the high normal stress was used corresponds to about 6 times the average grain size of the mineral components. Using an intermediate normal stress yielded microfractures with a maximum length up to 4 times the average grain size of the mineral components. Finally, under low normal stress conditions the maximum length of the microfractures was up to 2 times the average grain size of the mineral components.

6. Conclusions

Direct shear tests were carried out in this paper on sandstone joint samples subjected to three different values of normal stress. The AE in the samples was also monitored at the same time.

The following conclusions can be drawn from the study:

- (1) The characteristics of the ambient noise signals and rock fracture signals can be investigated and used to derive reasonable values for the AE threshold and sampling frequency used in the AE-monitoring system. The values chosen must ensure that the signals produced as the rock undergoes shear failure can be effectively detected and recorded. They must also ensure that the background noise is effectively eliminated
- (2) An expression can be established for the kinetic energy of the fracture surface using the AE information. The energy components involved in the failure process can then be analyzed. The results can be combined with the first law of thermodynamics to establish a method of calculating the scale of the tensile-shear fractures based on the AE data collected
- (3) The rock joints failure more extensively when a greater normal stress is applied. The rock joints simultaneously undergo shear failure in several localized regions of the joint surface. That is, the failure occurs synchronously in the different shear areas rather than sequentially
- (4) The average length of the microfractures generated in the process of shear failure is essentially consistent with the average size of the grains in the rock. However, the maximum length of the microfractures appears to vary with the normal stress applied. If the normal stress is high, the maximum length can be up to 6 times the average grain size. This falls to about 4 times if an intermediate normal stress is used and about 2 times if the normal stress is low

Abbreviations

| | |
|--------------|---|
| UCS: | Uniaxial compressive strength |
| E : | Young's modulus |
| G : | Shear modulus |
| ν : | Poisson's ratio |
| σ_t : | Tensile strength of rock |
| ρ : | Density of rock |
| ρ_c : | Density of coupling agent |
| V_p : | Elastic wave velocity in rock |
| V_c : | Elastic wave velocity in coupling agent |
| μ : | Effective friction coefficient |
| K_{II} : | Fracture toughness of type II |
| K_{IC} : | Fracture toughness of type I |
| n : | Porosity |
| JRC: | Joint roughness coefficient |
| E_i : | Internal energy |

| | |
|--|---|
| E_a : | Surface energy |
| E_d : | Dissipated energy |
| E_k : | Kinetic energy |
| L : | Distance between a microfracture source and AE sensor |
| R_p : | Propagation coefficient of a sensor |
| $\langle R_p \rangle$: | Average propagation coefficient of all sensors |
| θ_i : | Angle between the direction of elastic wave propagation and the normal to the sensor surface. |
| C_v : | Correction term of the volumetric component |
| $v(t)$: | Particle velocity waveform |
| t_d : | Duration of a signal |
| M : | Moment tensor |
| m_{11}, m_{22}, m_{33} : | Deviatoric eigenvalues of the matrix M |
| $\lambda_{\max}, \lambda_{\text{int}}, \lambda_{\min}$: | Eigenvalues of the matrix M |
| $u(x)$: | Amplitude of the signal |
| C_s : | Magnitude of the sensor response |
| (r_1, r_2, r_3) : | Direction vector from an AE source to the sensor |
| $u(t)$: | Voltage signal waveform |
| St : | Sensitivity of the sensor |
| RMS: | Root mean square (of a signal) |
| τ : | Shear stress |
| σ_n : | Normal stress |
| a, d : | Half-length and diameter of a microfracture. |

Data Availability

The AE-monitoring data and the shear test data during the study are available from the corresponding author upon reasonable request.

Conflicts of Interest

The authors declare that they have no known competing financial interests or personal relationships that could have appeared to influence the work reported in this paper.

Acknowledgments

The authors gratefully acknowledge the financial support from the National Natural Science Foundation of China (No. 42177168), the Project of Youth Innovation Promotion Association of Chinese Academy of Sciences (No. 2021326), the Systematic Project of Guangxi Key Laboratory of Disaster Prevention and Engineering Safety (No. 2019ZDK034), and the Open Research Fund of the State Key Laboratory of Geomechanics and Geotechnical Engineering, Institute of Rock and Soil Mechanics, Chinese Academy of Sciences (SKLGME021009).

References

- [1] N. Barton, "Review of a new shear-strength criterion for rock joints," *Engineering Geology*, vol. 7, no. 4, pp. 287–332, 1973.
- [2] Q. Jiang, B. Yang, F. Yan, C. Liu, Y. Shi, and L. Li, "New method for characterizing the shear damage of natural rock joint based on 3D engraving and 3D scanning," *International Journal of Geomechanics*, vol. 20, no. 2, article 6019022, 2020.
- [3] Y. Wang, H. N. Yang, J. Q. Han, and C. Zhu, "Effect of rock bridge length on fracture and damage modelling in granite containing hole and fissures under cyclic uniaxial increasing-amplitude decreasing-frequency (CUIADF) loads," *International Journal of Fatigue*, vol. 158, article 106741, 2022.
- [4] D. H. Chen, H. E. Chen, W. Zhang, J. Q. Lou, and B. Shan, "An analytical solution of equivalent elastic modulus considering confining stress and its variables sensitivity analysis for fractured rock masses," *Journal of Rock Mechanics and Geotechnical Engineering*, vol. 14, pp. 825–836, 2022.
- [5] S. Q. Duan, X. T. Feng, Q. Jiang, G. F. Liu, S. F. Pei, and Y. L. Fan, "In situ observation of failure mechanisms controlled by rock masses with weak interlayer zones in large underground cavern excavations under high geostress," *Rock Mechanics and Rock Engineering*, vol. 50, no. 9, pp. 2465–2493, 2017.
- [6] J. C. Zhang, Q. Jiang, G. L. Feng, S. J. Li, S. Pei, and B. He, "Geometrical characteristic investigation of the Baihetan irregular columnar jointed basalt and corresponding numerical reconstruction method," *Journal of Central South University*, vol. 29, no. 2, pp. 455–469, 2022.
- [7] H. Atapour and M. Moosavi, "The influence of shearing velocity on shear behavior of artificial joints," *Rock Mechanics and Rock Engineering*, vol. 47, no. 5, pp. 1745–1761, 2014.
- [8] G. L. Feng, B. R. Chen, Y. X. Xiao et al., "Microseismic characteristics of rockburst development in deep TBM tunnels with alternating soft-hard strata and application to rockburst warning: a case study of the Neelum-Jhelum hydropower project," *Tunnelling and Underground Space Technology*, vol. 122, article 104398, 2022.
- [9] Y. Yu, G. L. Feng, C. J. Xu, B. R. Chen, D. X. Geng, and B. T. Zhu, "Quantitative threshold of energy fractal dimension for immediate rock burst warning in deep tunnel: a case study," *Lithosphere*, vol. 2021, no. Special 4, article 1699273, 2022.
- [10] G. L. Feng, X. T. Feng, B. R. Chen, Y. X. Xiao, and Y. Yu, "A microseismic method for dynamic warning of rockburst development processes in tunnels," *Rock Mechanics and Rock Engineering*, vol. 48, no. 5, pp. 2061–2076, 2015.
- [11] S. F. Wang, X. B. Li, J. Yao et al., "Experimental investigation of rock breakage by a conical pick and its application to non-explosive mechanized mining in deep hard rock," *International Journal of Rock Mechanics and Mining Sciences*, vol. 122, article 104063, 2019.
- [12] S. Thirukumar, B. Indraratna, E. T. Brown, and P. K. Kaiser, "Stability of a rock block in a tunnel roof under constant normal stiffness conditions," *Rock Mechanics and Rock Engineering*, vol. 49, no. 4, pp. 1587–1593, 2016.
- [13] K. Monsen and N. Barton, "A numerical study of cryogenic storage in underground excavations with emphasis on the rock joint response," *International Journal of Rock Mechanics and Mining Sciences*, vol. 38, no. 7, pp. 1035–1045, 2001.
- [14] R. Gu and U. Ozbay, "Distinct element analysis of unstable shear failure of rock discontinuities in underground mining conditions," *International Journal of Rock Mechanics and Mining Sciences*, vol. 68, pp. 44–54, 2014.
- [15] H. B. Li, B. Liu, H. P. Feng, and L. Q. Zhang, "Study of deformability behaviour and failure mechanism by simulating rock joints sample under different loading conditions," *Rock and Soil Mechanics*, vol. 29, no. 7, p. 1741, 2008.

- [16] C. Grosse and M. Ohtsu, "Source Localization," in *Acoustic Emission Testing*. Springer Tracts in Civil Engineering, C. U. Grosse, M. Ohtsu, D. G. Aggelis, and T. Shiotani, Eds., Springer, Cham, 2008.
- [17] Z. A. Moradian, G. Ballivy, and P. Rivard, "Application of acoustic emission for monitoring shear behavior of bonded concrete-rock joints under direct shear test," *Canadian Journal of Civil Engineering*, vol. 39, no. 8, pp. 887–896, 2012.
- [18] H. Zhou, F. Meng, C. Zhang, D. Hu, J. Lu, and R. Xu, "Investigation of the acoustic emission characteristics of artificial saw-tooth joints under shearing condition," *Acta Geotechnica*, vol. 11, no. 4, pp. 925–939, 2016.
- [19] Y. Yu, D. C. Zhao, G. L. Feng, D. X. Geng, and H. S. Guo, "Energy evolution and acoustic emission characteristics of uniaxial compression failure of anchored layered sandstone," *Frontiers in Earth Science*, vol. 10, article 841598, 2022.
- [20] C. D. Zhang, W. G. Liang, Z. G. Li, S. G. Xu, and Y. S. Zhao, "Observations of acoustic emission of three salt rocks under uniaxial compression," *International Journal of Rock Mechanics and Mining Sciences*, vol. 77, pp. 19–26, 2015.
- [21] J. P. Liu, Y. H. Li, S. D. Xu, S. Xu, C. Y. Jin, and Z. S. Liu, "Moment tensor analysis of acoustic emission for cracking mechanisms in rock with a pre-cut circular hole under uniaxial compression," *Engineering Fracture Mechanics*, vol. 135, pp. 206–218, 2015.
- [22] M. Ohnaka and K. Mogi, "Frequency characteristics of acoustic emission in rocks under uniaxial compression and its relation to the fracturing process to failure," *Journal of Geophysical Research*, vol. 87, no. B5, pp. 3873–3884, 1982.
- [23] Z. A. Moradian, G. Ballivy, P. Rivard, C. Gravel, and B. Rousseau, "Evaluating damage during shear tests of rock joints using acoustic emissions," *International Journal of Rock Mechanics and Mining Sciences*, vol. 47, no. 4, pp. 590–598, 2010.
- [24] Y. Niu, X. P. Zhou, and F. Berto, "Temporal dominant frequency evolution characteristics during the fracture process of flawed red sandstone," *Theoretical and Applied Fracture Mechanics*, vol. 110, article 102838, 2020.
- [25] T. Z. Wang, L. X. Wang, F. Xue, and M. Y. Xue, "Identification of crack development in granite under triaxial compression based on the acoustic emission signal," *International Journal of Distributed Sensor Networks*, vol. 17, no. 1, 2021.
- [26] Q. Jiang, C. Liu, G. L. Feng, Y. Yang, H. Zheng, and C. B. Du, "Evolution of natural joints' mesoscopic failure modes under shear tests: acoustic emission investigation," *International Journal of Geomechanics*, vol. 21, no. 11, article 4021205, 2021.
- [27] S. F. Karimian, M. Modarres, and H. A. Bruck, "A new method for detecting fatigue crack initiation in aluminum alloy using acoustic emission waveform information entropy," *Engineering Fracture Mechanics*, vol. 223, article 106771, 2020.
- [28] P. Rodríguez and T. B. Celestino, "Application of acoustic emission monitoring and signal analysis to the qualitative and quantitative characterization of the fracturing process in rocks," *Engineering Fracture Mechanics*, vol. 210, pp. 54–69, 2019.
- [29] J. Pei, W. Fei, and J. Liu, "Spatial evolution and fractal characteristics of natural fractures in marbles under uniaxial compression loading based on the source location technology of acoustic emission," *Environmental Earth Sciences*, vol. 75, no. 9, p. 828, 2016.
- [30] R. D. Lei, Z. Y. Zhang, F. Berto, P. G. Ranjith, and L. Liu, "Cracking process and acoustic emission characteristics of sandstone with two parallel filled-flaws under biaxial compression," *Engineering Fracture Mechanics*, vol. 237, article 107253, 2020.
- [31] S. Shahidan, R. Pulin, N. Bunnori, and K. Holford, "Damage classification in reinforced concrete beam by acoustic emission signal analysis," *Construction and Building Materials*, vol. 45, pp. 78–86, 2013.
- [32] P. R. Prem, A. R. Murthy, and M. Verma, "Theoretical modelling and acoustic emission monitoring of RC beams strengthened with UHPC," *Construction and Building Materials*, vol. 158, pp. 670–682, 2018.
- [33] T. Yamada, J. J. Mori, S. Ide et al., "Stress drops and radiated seismic energies of microearthquakes in a South African gold mine," *Journal of Geophysical Research-Solid Earth*, vol. 112, no. B3, 2007.
- [34] P. Zhang, H. Liu, K. Guan, T. Xu, Q. Yu, and T. Yang, "A shear model for rock microfracture size estimation based on AE measurement," *Rock Mechanics and Rock Engineering*, vol. 54, no. 5, pp. 2533–2546, 2021.
- [35] C. H. Scholz, *The Mechanics of Earthquakes and Faulting*, Cambridge University Press, Cambridge, 3rd edition, 2018.
- [36] M. Cai, P. K. Kaiser, and C. D. Martin, "A tensile model for the interpretation of microseismic events near underground openings," *Pure and Applied Geophysics*, vol. 153, no. 1, pp. 67–92, 1998.